

# Development of High Sensitivity CMOS-MEMS Inertia Sensor and its Application to Early-Stage Diagnosis of Parkinson's Disease

Kazuya Masu\*, Daisuke Yamane\*, Katsuyuki Machida\*, Masato Sone\*, and Yoshihiro Miyake†,

\* FIRST, Institute of Innovative Research, Tokyo Institute of Technology, Yokohama, 226-8503 Japan

† Department of Computer Science, School of Computing, Tokyo Institute of Technology, Yokohama, 226-8503, Japan Tokyo

\*E-mail: masu.k.aa@m.titech.ac.jp

**Abstract**—In this paper, we present our recent progress of a high sensitivity complementary metal-oxide semiconductor-microelectromechanical systems (CMOS-MEMS) inertia sensor and its application to early-stage diagnosis of Parkinson's disease. The feature of the CMOS-MEMS sensor is the use of gold proof mass. High density of gold enables us to increase sensitivity by reducing thermo-mechanical noise that is inversely proportional to proof mass. We then show the developed CMOS-MEMS multi-physics design environment. An equivalent circuit of a MEMS accelerometer has been designed to simultaneously understand both the mechanical and the electrical behaviors. One of the potential applications of the high sensitivity inertia sensor is also discussed by focusing on early-stage diagnosis of Parkinson's disease.

**Keywords**—CMOS-MEMS; gold proof mass; inertia sensor; multi-physics design environment; Parkinson's disease

## I. INTRODUCTION

Microelectromechanical systems (MEMS) inertia sensors, such as MEMS accelerometers, are now widely used for a variety of applications as seen in automotive, industrial, healthcare, entertainment, consumer handheld electronics, and so forth [1]. The driving force behind the continuous performance improvement of MEMS inertia sensors is the development of silicon MEMS technology [2] with the use of surface micromachining process in combination with capacitive sensing methods [3]. The MEMS technology has enabled us to miniaturize all the mechanical components down to micro-meter scale and to reduce production cost by taking advantage of semiconductor manufacturing process.

Today, commercial MEMS inertia sensors accommodate typically more than 1 G ( $1\text{ G} = 9.8\text{ m/s}^2$ : gravitational acceleration). On the other hand, accurate sub-1G sensing by using MEMS inertial sensors has potential to realize various unexplored applications, such as precise monitoring of human and non-human objects for healthcare and medical purposes or integrated inertial measurement unit for advanced navigation systems [4].

So far, several MEMS accelerometers have been proposed to sense such a sub-1G range [5, 6], where they utilize a large-sized silicon proof mass to reduce the thermal-mechanical

noise, namely Brownian noise ( $B_N$ ). Such an approach would increase the MEMS device footprint and thereby the manufacturing cost.

In this paper, we first present our recent research progress of a high sensitivity CMOS-MEMS inertia sensor. Next, we show our CMOS-MEMS multi-physics design environment that enables to simulate both the mechanical and the electrical behavior of the inertia sensor. Lastly, a possible application of the inertia sensor is discussed in terms of early-stage diagnosis of Parkinson's disease.

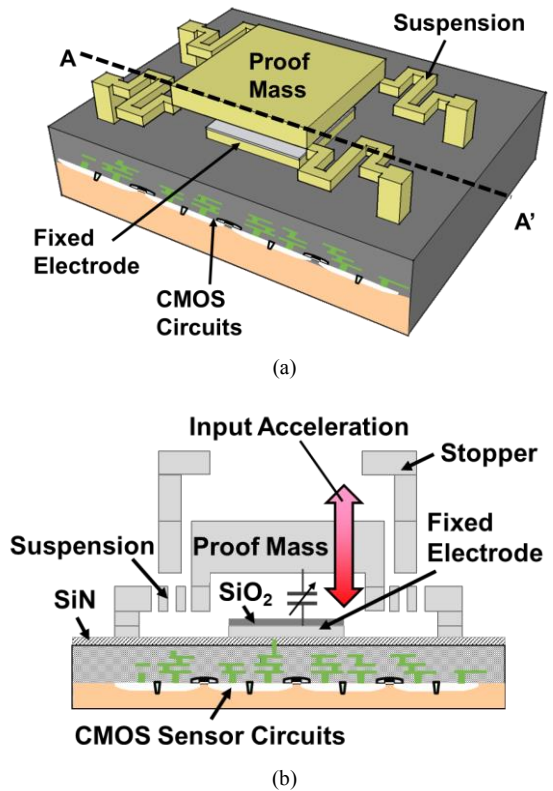


Fig. 1. Conceptual cross section of CMOS-MEMS accelerometer. (a) Bird-eye view and (b) cross-section image.

## II. HIGH SENSITIVITY INERTIA SENSOR USING GOLD AS PROOF-MASS

Figure 1 shows the conceptual image of the developed CMOS-MEMS inertia sensor. The MEMS structure is fabricated onto standard CMOS wafer using so-called post-CMOS process [7]. The feature of the MEMS device is the use of a gold proof mass, which contributes to reduce the  $B_N$  in the inertia sensor. The  $B_N$  of moving structures determines the sensitivity of MEMS accelerometer.  $B_N$  is expressed as

$$B_N = \frac{\sqrt{4k_B T b}}{m} \quad (1)$$

where  $k_B$ ,  $T$ ,  $b$  and  $m$  are the Boltzmann constant ( $1.38 \times 10^{-23}$

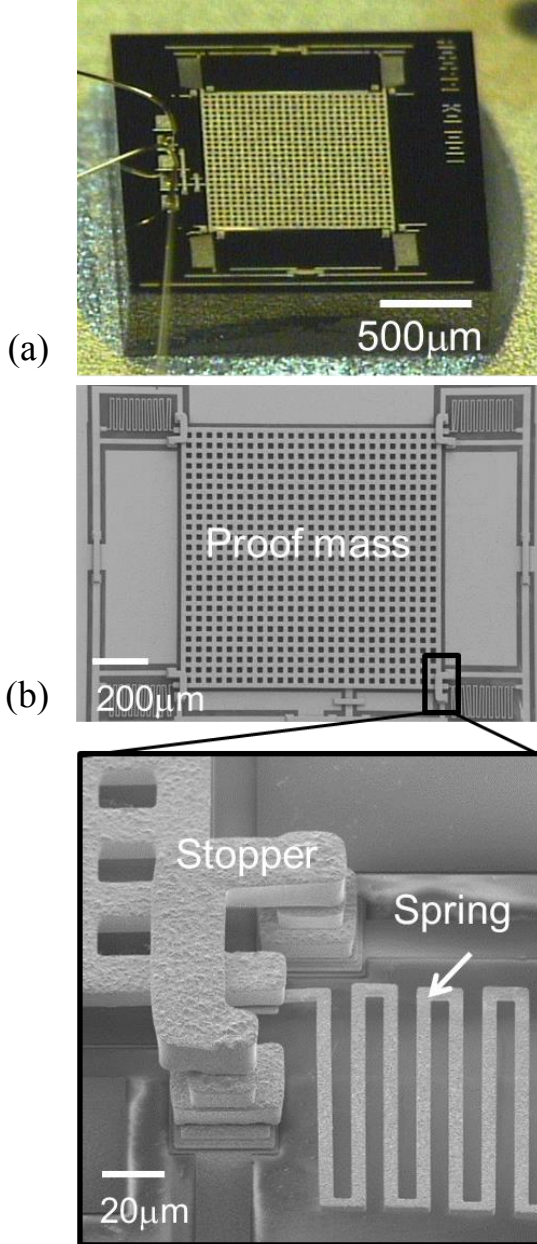


Fig. 2. Sub-1G MEMS inertia sensor with a high-density proof mass [10]. (a) Chip photo and (b) SEM images. The thickness of Au proof mass is 12  $\mu\text{m}$ .

J/K), the absolute temperature, the viscous damping coefficient and the mass of the movable structures of an inertial sensor, respectively. From eq. (1), increasing the density of the proof mass is an effective and straightforward way to suppress the  $B_N$  without compromising the device footprint. The reason of the use of gold is that the density of Au ( $19.3 \times 10^3 \text{ kg/m}^3$  at RT) is nearly an order of magnitude higher than that of Si ( $2.33 \times 10^3 \text{ kg/m}^3$  at RT) [8] used as a standard material of proof mass.

Figure 2 is a fabricated sub-1G inertia sensor with the scanning electron microscope (SEM) images. The designed  $B_N$  was  $0.12 \mu\text{G/Hz}^{1/2}$ . From the measured values of the mechanical resonant frequency and the mechanical Q,  $B_N$  was estimated to be below  $1 \mu\text{G/Hz}^{1/2}$ , which was sufficiently below the target value of  $10 \mu\text{G/Hz}^{1/2}$  [9, 10]. We also confirmed that the sub-1G MEMS inertia sensor can function without mechanical failure after the input acceleration of up to 20 G [11], as shown in Fig. 3.

The gold layer which was used for the MEMS inertia sensor were deposited by electroplating method. Ti/Au cantilevers were fabricated for evaluating the structure stability as shown in Fig. 4 [12, 13]. Clear yielding was not observed in even 3  $\mu\text{m}$ -thick  $\times$  10  $\mu\text{m}$ -wide with 1,000  $\mu\text{m}$ -long cantilever.

The mechanical properties such as yield strength, Young modulus, stability, etc. are important parameters for designing MEMS structures. High mechanical properties of nanocrystalline Au have been investigated [14][15].

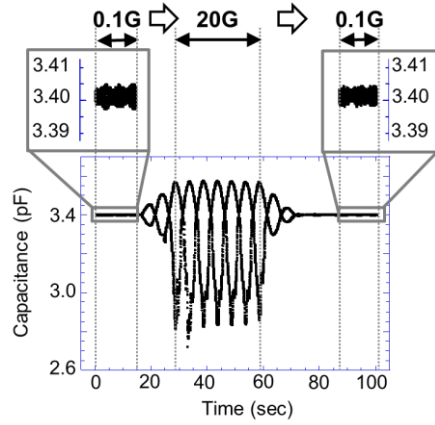


Fig. 3. Measured capacitance response of sub-1G sensor at the input acceleration from 0.1 G to 20 G [12].

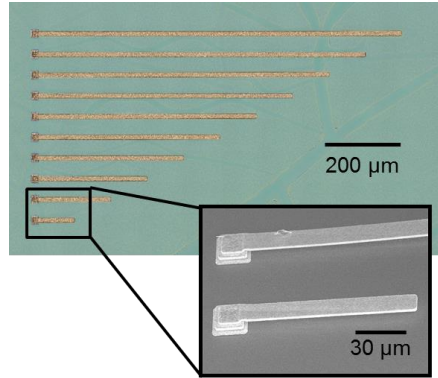


Fig. 4. Ti/Au multi-layer metal micro cantilevers with 3  $\mu\text{m}$ -thick Au [12].

Three types of electroplating Au film were prepared. (1) the conventional constant-current electroplating (CE) using a cyanide-based electrolyte, (2) CE using sulfite-based electrolyte, and (3) the pulse electroplating (PE) with a sulfite-based electrolyte. After the electroplating, micro-pillars were made from the Au films by focused ion beam milling. Dimensions of the fabricated pillars were  $10\mu\text{m} \times 10\mu\text{m} \times 20\mu\text{m}$ .

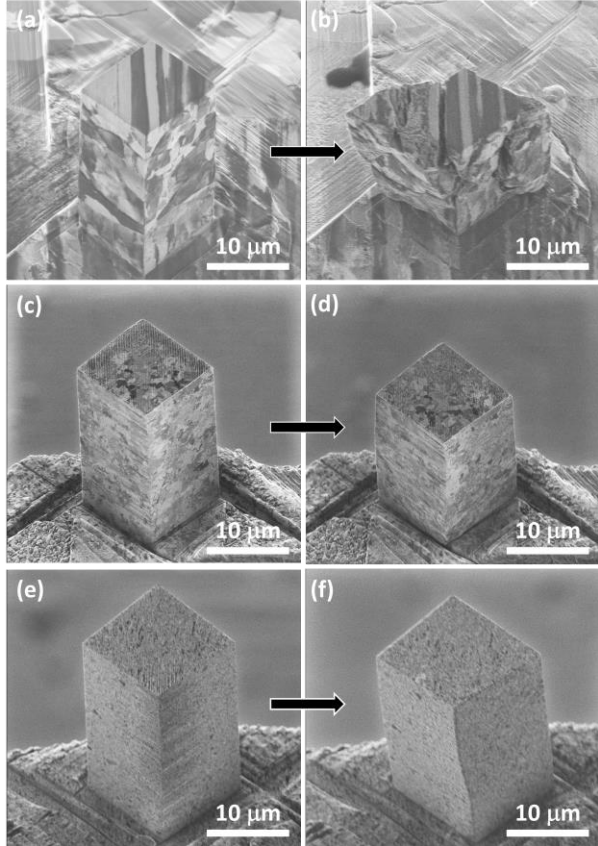


Fig. 5 SIM images of the (a) as-fabricated and (b) deformed Au pillars fabricated from the CE with the cyanide-based electrolyte, the (c) as-fabricated and (d) deformed Au pillars fabricated from the CE with the sulfite-based electrolyte, and the (e) as-fabricated and (f) deformed Au pillars fabricated from the PE with the sulfite-based electrolyte. [14]

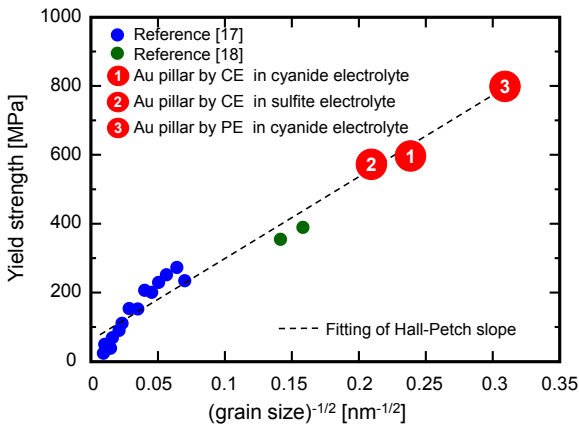
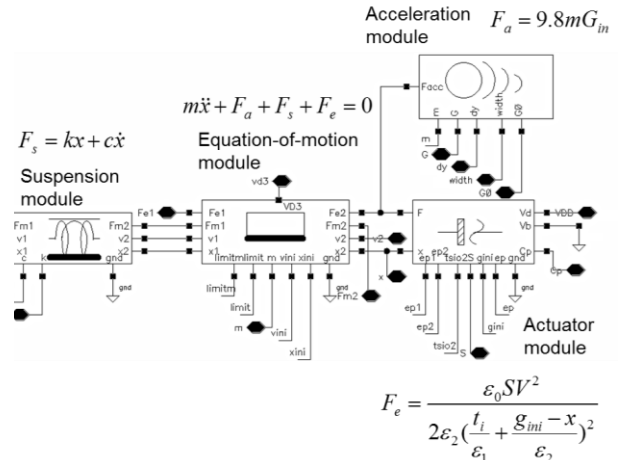


Fig. 6 Hall-Petch plot of polycrystalline Au pillars [14]. The yield strength of poly-Si is known to be a few GPa.

The Au pillar by CE-Cy of Fig. 5(a) has the columnar textures with a direction perpendicular to the substrate/electrolyte interface. The grain size obtained from XRD was 17.6 nm. Cracks in Fig. 5(b) indicate brittle fractures along the texture boundary, which suggest the brittle nature of the texture boundary. The Au pillar of CE-Su of Fig. 5(c) has camouflage pattern of the grain/structure on the surface. After ca.10% deformation, the Au pillar shows broad shear crossing from the top front to the bottom as shown in Fig. 5(d). The Au pillar by PE-Su of Fig. (e) has no obvious grain/textured boundary, and the grain size was 10.5nm. The ductile deformation shown in Fig. 5(f) was attributed to the intrinsic property of ultra-fine or nanocrystalline materials during the compressive deformation. Although the grain size was different between the micro-pillars fabricated from the CE-Su and the PE-Su, the deformation behaviors were similar as shown in Figs. 5(d) and (f). Figure 6 shows Hall-Petch plot of Au pillars. The yield strength was obtained from the compressive engineering stress strain curves of the Au pillars [14]. The strengths obtained in this work well followed the Hall-Petch relationships and reached 800 MPa. To the best of our knowledge a compressive strength of 800 MPa is the highest value reported for electrodeposited pure Au when compared with the literatures [16-18]. Also, the Au film prepared by the PE had large work hardening which indicates high ductility and malleability of the material. These results can sweep out the gloomy anxiety that Au is soft and cannot be available MEMS structure.

### III. DEVELOPMENT OF CMOS-MEMS MULTI-PHYSICS DESIGN ENVIRONMENT

The reason why large-scale integrated circuit (LSI) designer can design the circuit is that design environment and design kit are provided to the designer. We have developed CMOS-MEMS multi-physics design environment [19]. Figure 7 shows an equivalent circuit of a MEMS capacitive accelerometer for the multi-physics design environment. The equivalent circuit consists of five modules; i) an actuator module to read out the electrostatic force  $F_e$  as a function of applied voltage  $V$ . ii) a suspension module for the viscoelastic restoring force  $F_s$ , iii) an acceleration module to calculate the inertia force  $F_a$ , iv) an equation-of-motion module to calculate



MOS-MEMS multi-physics simulation design environment [14].

the velocity and displacement  $x$  of proof mass as a result of impinging force, and v) and anchor module to fix the mechanical ends. These modules are described by a Verilog-A compatible hardware description language (HDL). Multi-physics simulation is performed by SPICE on usual LSI design environments. CMOS and MEMS layouts are also designed on the multi-physics design environment.

Figure 8 is an example of CMOS-MEMS co-simulation and measurement results. The output voltages as a function of the input acceleration were obtained by multi-physics simulation and experiments. The behavior model had a good agreement with the experimental results for the input acceleration of 3 G or lower. For the input acceleration of 3 G or larger, notable

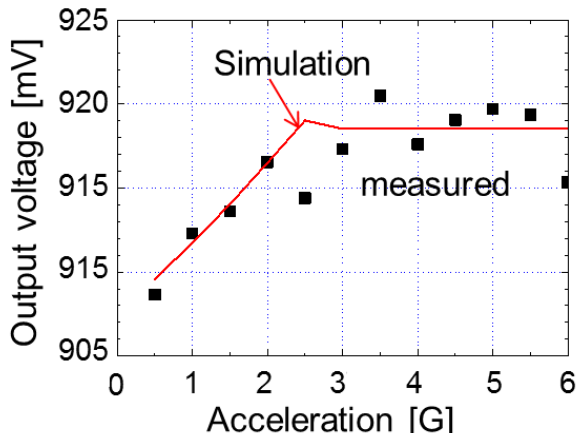


Fig. 8. CMOS-MEMS multi-physics simulation. MEMS inertia sensor on 0.35 mm standard CMOS [14].

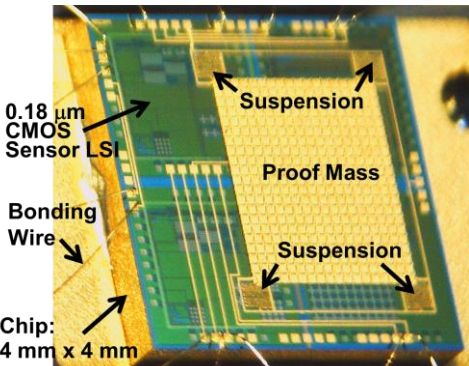


Fig. 9. Chip photo of CMOS-MEMS integrated inertia sensor [20].

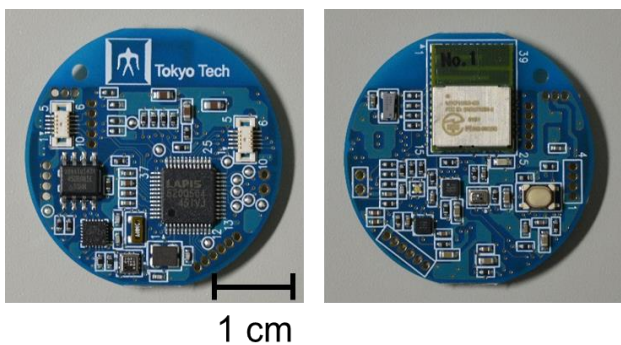


Fig. 10. A sensor module with Bluetooth low energy wireless communication.

deviations were found in the experimental results possibly due to excess mechanical motion of the proof mass ramming in the suspensions and the substrate. Figure 9 is a photo of a recently developed CMOS-MEMS inertia sensor [20]. The sensor LSI was fabricated with 0.18-μm CMOS process, and the MEMS structures were successfully implemented onto the LSI chip with the footprint of  $4 \times 4 \text{ mm}^2$  by the post-CMOS process [7].

Lately, we have developed sensor module using Bluetooth low energy as shown in Fig. 10. The several sensors such as temperature, pressure, accelerometer, gyroscope and so forth, are integrated on the module. This small size module is used for human motion sensing. The high sensitivity inertia sensor will be implemented on this module.

#### IV. EARLY STAGE DIAGNOSIS OF PARKINSON'S DISEASE

Parkinson's disease is originated from lack of dopamine secretion. Early-stage diagnosis enables the delay of symptom progress and/or the interval extension of Levodopa dosing, resulting in quality-of-life (QoL) improvement of Patient. Parkinson's disease is categorized by Hoehn-Yahr (HY) scale as shown in Fig. 11. We have reported HY2-3 diagnosis from the analysis of walking period with around 80 % accuracy [21-29]. In this paper, preliminary results of earlier diagnosis using inertia sensors in terms of patients' postural reflex failure.

Postural abnormality is one of the symptoms of Parkinson's disease. X-ray image, floor reaction sensor and motion capture system are used to evaluate this. Estimation postural angle by using compact accelerometers yields benefits that it reduces environmental limit and realizes lifelog. Therefore, we developed quantitative evaluation system using accelerometers for postural abnormality in Parkinson's disease. The proposal

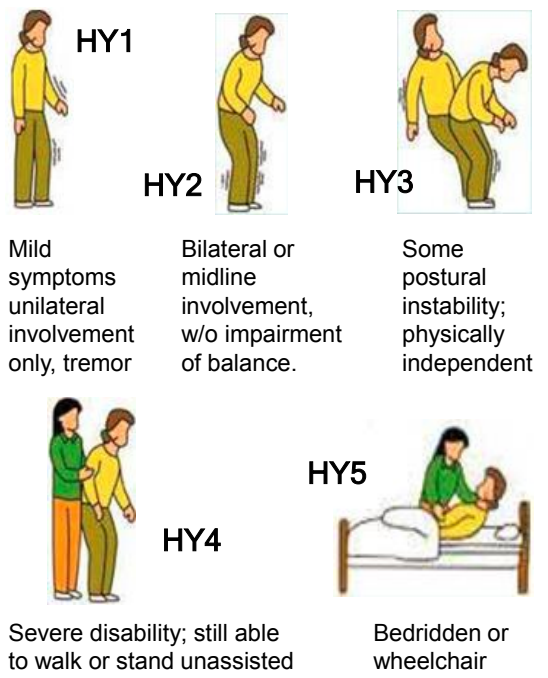


Fig. 12. Hoehn-Yahr (HY) scale of Parkinson's disease.

system is composed of postural angle estimation, postural feature extraction and PD classification.

The proposal system consists of two sensor modules. The patients wear one of the sensor on 10cm below C7 vertebra and the other on L4 vertebra. Postural angles of each sensor are estimated by the gravity components of accelerations. The algorithm is summarized in Fig. 12.

17 healthy young people, 17 healthy elderly people, 19 mild PD, HY 1-2, patients and 24 severer PD, HY 2.5-4, patients were participated in this experiment. All participants' postural angles were measured under 3 conditions, sitting, standing and walking by the proposal system. The result under the standing condition is shown in Fig. 13.

150 features such as range, average, variance and skewness are extracted from measured accelerations data. To find effective features for PD classifier, we compared the features of each group, healthy young, healthy elderly, mild PD and severe PD. 41 features are significant difference ( $p < 0.01$ , Kruskal-Wallis test). Figure 14 shows the result of comparison.

Finally, we constructed classifiers by using these feature values. In this work, Support Vector Machines are used for classification. Cross-validation is used to verify the constructed classifiers. The result shown in Table I. We will continue the earlier diagnosis in terms of patients' tremor (vibration of fingers and hands) using high-sensitivity inertia sensors.

## V. CONCLUSION

We presented our recent progress of a high sensitivity CMOS-MEMS inertia sensor and discussed the sensor application to the diagnosis of Parkinson's disease. The experiment results show the inertia sensor has high potential for sensing sub-1G acceleration. The preliminary earlier diagnosis using inertia sensors was demonstrated. We then conclude that the proposed high sensitivity inertia sensor can be a key component to realize early-stage diagnosis system for Parkinson's disease.

## ACKNOWLEDGMENT

Part of this work is performed under JST-CREST. The authors would like thank JST financial support. The authors would like to thank Tokyo Tech CREST-team members, especially Prof. N. Ishihara, Prof. S. Dosho and Associate Prof. H. Ito for technical discussion. We also would like to thank Dr. T. Konishi with NTT Advanced Technology Corp. and Prof. H. Toshiyoshi with The University of Tokyo for useful discussion and suggestions. suggestions.

## REFERENCES

- [1] G. Krishnan, C. U. Kshirsagar, G. K. Ananthasuresh, and N. Bhat, "Micromachined High-Resolution Accelerometer," *J. Indian Inst. Sci.*, vol. 87, no. 3, pp. 333-361, Sept. 2007.
- [2] K. E. Petersen, "Silicon as a mechanical material," *Proc. IEEE*, vol. 70, issue 5, pp. 420-457, May 1982.
- [3] B. E. Boser and R. T. Howe, "Surface micromachined accelerometers," *IEEE J. Solid-State Circuits*, vol. 31, issue 3, pp. 366-375, Mar. 1996.

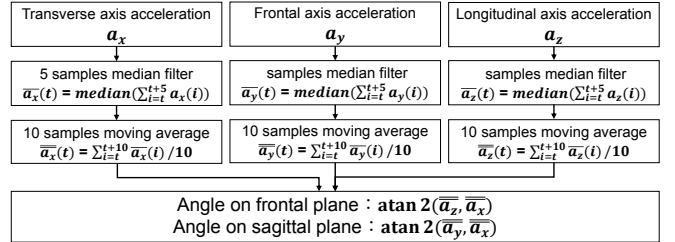


Fig. 12. The algorithm to estimate postural angles from acceleration data.

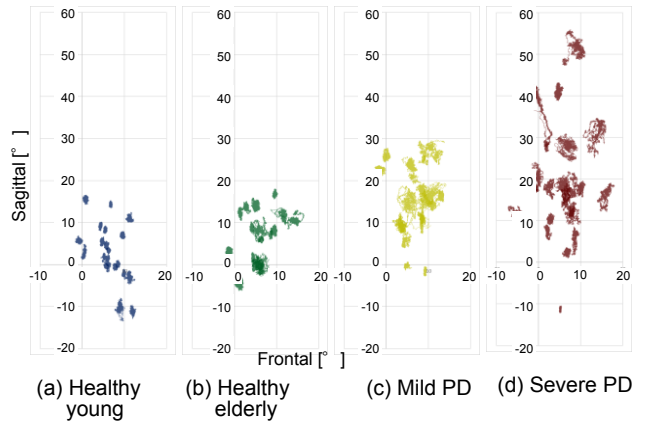


Fig. 13. Postural angles of 10cm below C7 during 30sec under the standing condition of each participant.

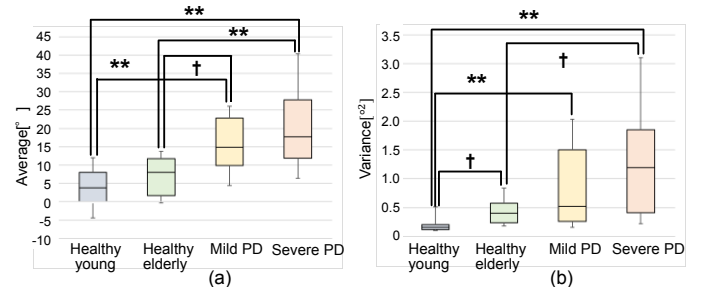


Fig. 14. Postural feature values. (a) Average of sagittal angle on 10cm below C7. (b) Variance of sagittal angle on 10cm below C7. † :  $p < 0.1$ , \* :  $p < 0.05$ , \*\* :  $p < 0.01$ , Steel-Dwass test.

TABLE I. THE CLASSIFIER'S ACCURACY EVALUATED BY CROSS-VALIDATION

	Accuracy [%]
Severe PD-Mild PD	81.0
Severe PD-Healthy Elderly	90.0
Mild PD-Healthy Elderly	77.8
Severe PD-Healthy Young	92.9
Mild PD-Healthy Young	89.5
Healthy Elderly-Healthy Young	80.6

- [4] N. Yazdi, F. Ayazi, and K. Najafi, "Micromachined Inertial Sensors," Proc. IEEE, vol. 86, issue 8, pp. 1640-1659, 1998.
- [5] J. Chae, H. Kulah, and K. Najafi, "A monolithic three-axis micro-g micromachined silicon capacitive accelerometer," IEEE J. Microelectromech. Syst., vol. 14, issue 2, pp. 235-242, April 2005.
- [6] R. Abdolvand, B.V. Amini, and F. Ayazi, "Sub-Micro-Gravity In-Plane Accelerometers With Reduced Capacitive Gaps and Extra Seismic Mass," IEEE J. Microelectromech. Syst., vol. 16, issue 5, pp. 1036-1043, Oct. 2007.
- [7] K. Machida, T. Konishi, D. Yamane, H. Toshiyoshi, and K. Masu, "Integrated CMOS-MEMS Technology and Its Applications," ECS Trans., vol. 61, issue 6, pp. 21-39, May 2014.
- [8] D. R. Lide, CRC Handbook of Chemistry and Physics, 75th ed., CRC Press, Inc., Florida, 1994.
- [9] D. Yamane, T. Konishi, H. Toshiyoshi, K. Masu, and K. Machida, "Design of sub-1g microelectromechanical systems accelerometers," Appl. Phys. Lett., vol. 104, issue 7, pp. 074102, 2014.
- [10] D. Yamane, T. Konishi, H. Toshiyoshi, K. Masu, and K. Machida, "A Sub-1G MEMS Sensor," (invited) in Proc. The 227<sup>th</sup> ECS Meeting, the Hilton Chicago, Chicago, Illinois, USA, May 22-28, 2015, pp. 1332.
- [11] D. Yamane, T. Konishi, T. Matsushima, H. Toshiyoshi, K. Masu, and K. Machida, "A 0.1G-to-20G Integrated MEMS Inertial Sensor," Jpn. J. Appl. Phys., vol. 54, no. 8, 2015, pp. 087202.1-087202.4.
- [12] D. Yamane, T. Konishi, M. Teranishi, T.-F. M. Chang, C.-Y. Chen, H. Toshiyoshi, K. Masu, M. Sone, and K. Machida, "A Study on Mechanical Structure of a MEMS Accelerometer Fabricated by Multi-layer Metal Technology," in Proc. 32nd Advanced Metallization Conference (AMC2015), Sept. 9-11, 2015, University of Texas at Austin, Austin, Texas, US.
- [13] M. Teranishi, T.-F. M. Chang, C.-Y. Chen, T. Konishi, K. Machida, H. Toshiyoshi, D. Yamane, K. Masu, and M. Sone, "Structure Stability of High Aspect Ratio Ti/Au Two-Layer Cantilevers for Applications in MEMS Accelerometers," Microelectronics Engineering, vol. 159, 2016, pp.90-93.
- [14] C.-Y. Chen, M.Yoshiba, T. Nagoshi, T.-F. M. Chang, D. Yamane, K. Machida, K. Masu, M. Sone, "Pulse Electroplating of Ultra-Fine Grained Au Films with High Compressive Strength" Electrochemistry Communication, vol.67, 2016, pp. 51-54
- [15] M.Yoshiba, C.-Y. Chen, T.-F. M. Chang, T. Nagoshi, D. Yamane, K. Machida, K. Masu, M. Sone, "Brittle Fracture of Electrodeposited Gold Observed by Micro-Compression" Materials Transactions, 2016, in press [doi:10.2320/matertrans.MG201612]
- [16] B. Bozzini, A. Fanigliulo, M. Serra, "Electrodeposition of star-shaped gold crystallites", J. Cryst. Growth vol.231, 2001, pp. 589-598.
- [17] Z. Gan, Y. He, D. Liu, B. Zhang, L. Shen, Hall-Petch effect and strain gradient effect in the torsion of thin gold wires, Scripta Materialia 87 (2014) 41-44.
- [18] R. D. Emery, G. L. Povirk, Tensile behavior of free-standing gold films. part II. fine-grained films, Acta Materiaria 51 (2003) 2079–2087.
- [19] T. Konishi, D. Yamane, T. Matsushima, K. Masu, K. Machida, and H. Toshiyoshi, "A capacitive CMOS-MEMS sensor designed by multi-physics simulation for integrated CMOS-MEMS technology," Jpn. J. Appl. Phys., vol. 53, no. 4S, 2014, pp. 04EE15.1-7.
- [20] T. Konishi, D. Yamane, M. Takayasu, H. Ito, S. Dosho, N. Ishihara, K. Masu, H. Toshiyoshi, and K. Machida, "Novel Gain-Controlled Sensor Circuits Designed by Multi-physics Simulation for CMOS-MEMS Accelerometer," in Proc. 2015 International Conference on Solid State Devices and Materials (SSDM 2015), Sapporo Convention Center, Sapporo, Japan, Sept. 27-30, 2015, pp. 798-799.
- [21] Y. Miyake, "Interpersonal synchronization of body motion and the Walk-Mate walking support robot," IEEE Trans. Robot., vol. 25, issue 3, pp. 638-644, June 2009.
- [22] M. J. Hove, K. Suzuki, H. Uchitomi, S. Orimo, and Y. Miyake, "Interactive rhythmic auditory stimulation reinstates natural 1/f timing in gait of Parkinson's patients," PLoS ONE, vol. 7, issue 3, pp. e32600, March 2012.
- [23] H. Uchitomi, L. Ota, K. Ogawa, S. Orimo, and Y. Miyake, "Interactive rhythmic cue facilitates gait relearning in patients with Parkinson's disease," PLoS ONE, vol. 8, issue 9, pp. e72176, Sep. 2013.
- [24] L. Ota, H. Uchitomi, K. Ogawa, S. Orimo, and Y. Miyake, "Relationship between neural rhythm generation disorders and physical disabilities in Parkinson's disease patients' walking," PLoS ONE, vol. 9, issue 11, pp. e112952, Nov. 2014.
- [25] L. Ota, K. Ogawa, M. S. R. Yap, and Y. Miyake, "Evaluation platform of gait rhythm in relation to movement disorder and sensorimotor interaction," in Proc. of the SICE Annual Conference 2014 (SICE 2014), Sapporo, Japan, pp. 856-859, Sep. 2014.
- [26] L. Ota, K. Ogawa, S. Orimo, and Y. Miyake, "Relation of postural instability to gait dynamics in patients with Parkinson's disease," in Proc. on ICME/CME 2014, Taipei, Taiwan, pp. 195-200, June 2014.
- [27] L. Ota, H. Hashiguchi, H. Uchitomi, K. Ogawa, S. Orimo, and Y. Miyake, "The Effect of Gait Training Using Interactive Rhythmic Auditory Stimulation on Parkinson's Disease Patients," in Proc. of the 2015 IEEE/SICE Int. Symp. on System Integration (SII 2015), Nagoya, Japan. (in press)
- [28] L. Ota, H. Hashiguchi, K. Ogawa, S. Orimo, and Y. Miyake, "Gait state transition by interactive rhythmic auditory cue in development process of gait rhythm generation disorders," in Proc. of the SICE Annual Conference 2015 (SICE 2015), Hanzhou, China, pp. 1485-1488, 2015.
- [29] L. Hashiguchi, K. Ogawa, S. Orimo, and Y. Miyake, "Gait state transition by interactive rhythmic auditory cue in development process of gait rhythm generation disorders," in Proc. on ICME/CME 2015, Okayama & Kyoto, Japan, pp. 41-46, June 2015.